Surface deformation from persistent scatterers SAR interferometry and fusion with leveling data: A case study over the Choushui River Alluvial Fan, Taiwan

Wei-Chia Hung [a], Cheinway Hwang [b,*], Yi-An Chen [a], Chung-Pai Chang [c], Jiun-Yee Yen [d], Andrew Hooper [e], Chin-Yi Yang [a]

[a] Green Energy and Environment Research Laboratories, Industrial Technology Research Institute, Bldg. 24, 195 Sec. 4, Chung Hsing Rd., Chutung, Hsinchu 310, Taiwan
[b] Department of Civil Engineering, National Chiao Tung University, 1001 Ta Hsueh Rd., Hsinchu 300, Taiwan
[c] Department of Earth Sciences and Institute of Geophysics, National Central University, No. 300, Jhongda Rd., Jhongli City, Taoyuan 320, Taiwan
[d] Institute of Earth Sciences, National Dong Hwa University, No. 123, Huasi Rd., Hualien 970, Taiwan
[e] Department of Earth Observation and Space Systems, Delft University of Technology, Kluyverweg 1, 2629 HS, 2600 GB Delft, Netherlands

A B S T R A C T

The Choushui River Alluvial Fan (CRAF), one of the most important agricultural areas in Taiwan, suffers severe subsidence caused by groundwater withdrawal. We use 20 ENVISAT images from 2006 to 2008 to derive vertical deformation over CRAF by persistent scatterer interferometry (PSI), which effectively reduces errors affecting conventional DInSAR techniques. The pixel density over CRAF is 107.6 pixels/km^2, compared to 0.19 points/km^2 of the leveling benchmarks. PSI yields vertical displacements matching the leveling result to 0.6 cm/year (RMS), and provides a higher spatial resolution of subsidence than the latter. We also develop a data fusion method that considers the high-precision, low point-density leveling result as a smoothed correction to the PSI result. The combined field is more representative of overall deformation characteristics than the PSI-only or leveling-only field, and it is better suited for the assessment of the impact of subsidence over CRAF.

© 2010 Elsevier Inc. All rights reserved.

1. Introduction

Many countries in the world suffer from severe land subsidence problems. Table 1 lists selected countries at selected periods of time with such problems. The major causes of subsidence in these countries are growing demands of water resources that prompt the need to extract groundwater. Global warming and increasing populations deepen the problems. Taiwan is among the countries with severe land subsidence problems, partly due to rapid economic developments that increase the demand for water resources. In particular, over-pumping of groundwater in the western plains of Taiwan (NYUST, 2009), facilitated by its easy access, has caused large-scale land subsidence in the southwestern coastal region. One area attracting public attention is the Choushui River Alluvial Fan (CRAF), which is the most important agricultural area in western coastal Taiwan. Fig. 1 shows the geographic location of CRAF which includes part of Yunlin County. Here the soil composition is relatively weak and the subsidence is larger than in other parts of CRAF. Because the Taiwan High Speed Rail (THSR) passes through Yunlin, land subsidence is a major safety concern. As such, effective monitoring

of subsidence has become a major social, economic and political issue in Taiwan.

Over CRAF, subsidence results based on leveling, GPS and multi-level compaction wells have been obtained that depict the patterns, linear trends and mechanisms of the subsidence (Hwang et al., 2008). Fig. 2 shows the current distribution of the stations of leveling, GPS and compaction wells. In total, there are 586 benchmarks (length of leveling route: 830 km), 8 continuous GPS stations, and 29 multi-level compaction monitoring wells. Leveling, GPS and compaction monitoring wells provide point observations, which combine to yield an average point density of 0.29 points/km^2. Between observation points, interpolation of subsidence is highly uncertain because of the low point density. The low spatial density may be mitigated by observations from space-borne techniques such as differential radar interferometry (DInSAR). However, DInSAR measurements are subject to uncertainties caused by the atmosphere-induced error, satellite orbit error and terrain effect. Also, CRAF is covered by paddy fields having different surface properties over different seasons, which cause spatial de-correlation in DInSAR leading to a degraded accuracy in the deformation measurements (Hung et al., 2010). This deficiency in DInSAR can be reduced by the persistent scatterer interferometry (PSI) technique (Hooper et al., 2004) or the SBAS technique (Berardino et al., 2002). In this paper, we will employ PSI to overcome the limitations of the conventional DInSAR technique for land deformation monitoring over CRAF. In addition, an optimal field of

* Corresponding author.
E-mail address: cheinway@mail.nctu.edu.tw (C. Hwang).

Table 1
A list of world countries experiencing subsidence problems.

Area	Geology condition	Maxima cumulative subsidence (m)	Period	Reference
Indonesia (Jakata)	Pleistocene marine facies and Cenozoic alluvia deposits	2.0	1982–1997	Abidin et al. (2001)
USA (Las Vegas)	Late Tertiary and Quatemary lacustrine, paludal, and alluvial deposits	0.2	1992–1997	Amelung et al. (1999)
USA (Texas)	Gulf Coast Aquifer System	3.0	1906–2000	Gabrysch and Ronald (2005)
China (Shanghai)	Quaternary alluvia deposits	3.0	1921–2006	Gong and Yang (2008)
USA (California)	Alluvia deposits	3.9	1916–1969	Hanson et al. (2005)
Taiwan (Taipei)	Quaternary alluvia deposits	2.1	1950–2007	Hung and Liu (2007)
China (Taiyuan)	Alluvia and latchstring deposits	2.9	1950–2003	Ma et al. (2006)
Iran (Mashhad)	Quaternary-Neogene alluvial deposits	0.96	1995–2005	Motagh et al. (2007)
Thailand (Bangkok)	Holocene fluvial and marine deposits	0.8	1978–2003	Noppadol et al. (2006)
Mexico (Mexico)	Quaternary lacustrine and alluvial-pyroclastic deposits	0.7	2004–2006	Osmanoglu et al. (2010)
Japan (Tokyo)	Pliocene and Pleistocene sediments	4.5	1918–2003	Sato et al. (2006)
Italy (Venice)	Quaternary marine facies, lagoon and alluvia deposits	0.5	1897–1937	Tosi et al. (2007)

surface deformation will be one that is based on measurements of varying spatial and temporal resolutions. Thus, we will also develop a method to combine the results from space-borne (SAR) and terrestrial (leveling) measurements.

2. Surface deformation by persistent scatterer SAR interferometry: application of StaMPS/MTI

Conventional DInSAR has become a popular method to measure surface deformation over a large area. The method is proved successful in many cases, particularly for measuring co-seismic deformation, where the magnitude of deformation can be up to several meters, see Chang et al. (2004) and Hashimoto et al. (2009). However, DInSAR is often affected by temporal de-correlation of radar signals, especially over terrain with dense vegetation or temporal variations in coverage such as for rice-paddy fields in central Taiwan. Errors in satellite orbits, atmospheric models and DEMs add to the uncertainty in DInSAR, even with coherent radar signals. It has been proposed to utilize only radar signals from stable targets to reduce the problems associated with temporal de-correlation and other errors. For example, Ferretti et al. (2000, 2001) first proposed a permanent scatterer (PS) method that identifies PS based on the amplitude dispersion index of radar signals
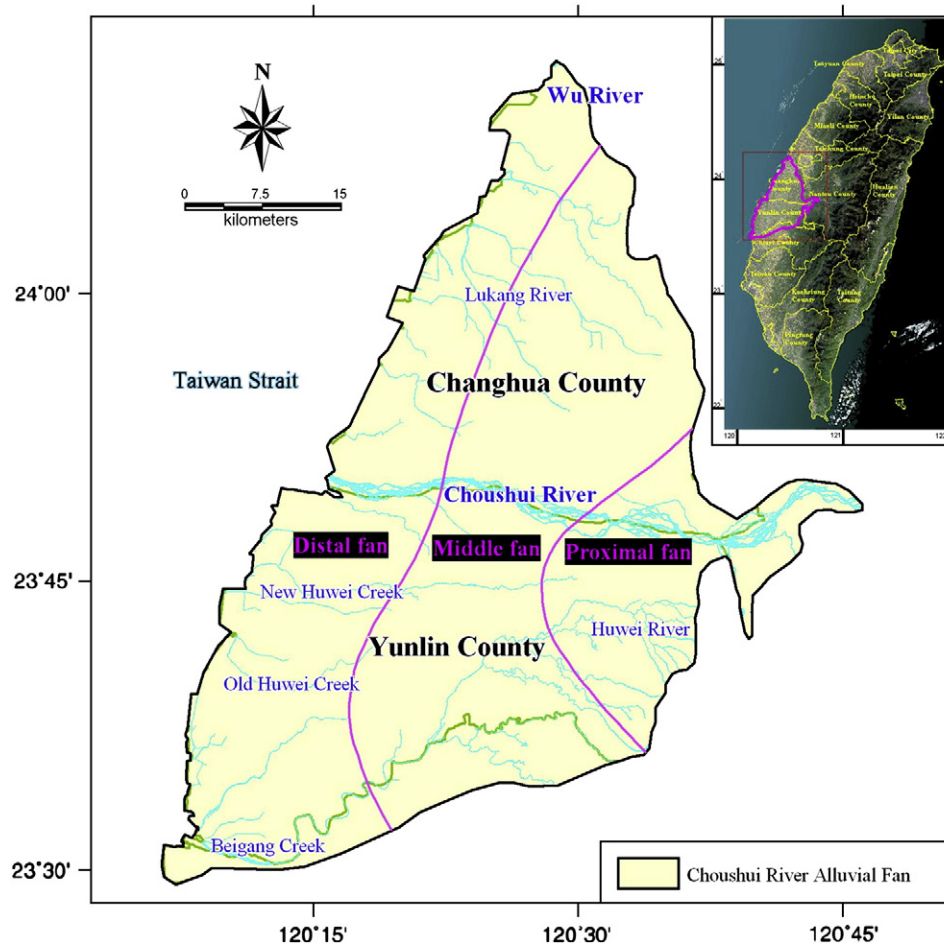

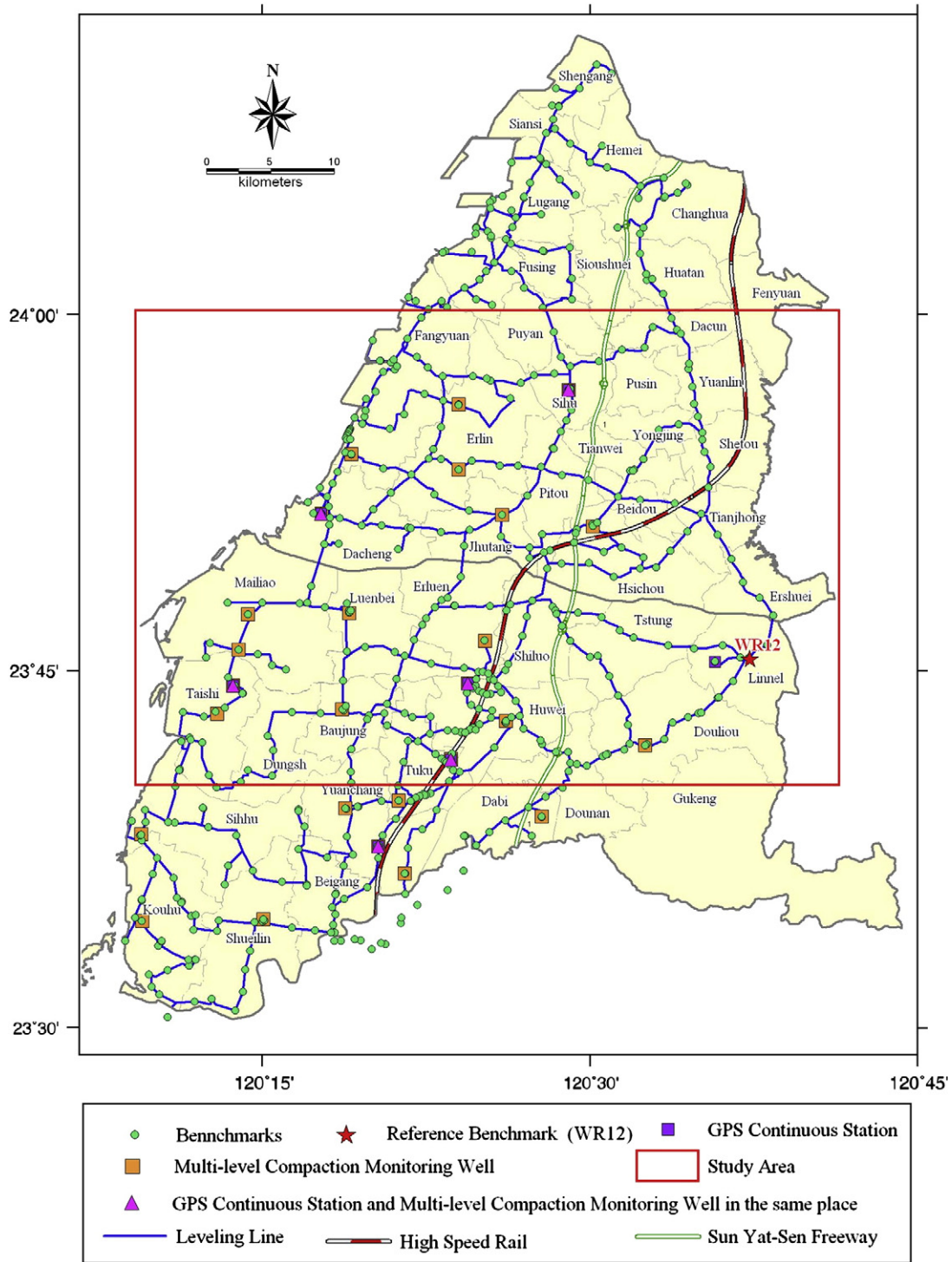**Fig. 1.** Geographical location of Choushui River Alluvial Fan (CRAF).

Fig. 2. Distributions of leveling benchmarks, monitoring wells and GPS stations in CRAF, the names of townships in Yunlin County and Changhua County are shown here. WR12 is the control benchmark for leveling. The red box covers the land area where PS pixels are identified.

(see below). Such a PS technique and its variant were subsequently used by, e.g., Lyons and Sandwell (2003) and Kampes (2005). These PS methods have been very successful in urban areas with many man-made objects. Because CRAF is mainly covered by rice paddies and fish ponds, there are very few man-made objects or stable targets. Obtaining sufficiently large amount of PS pixels here is critical to the success of the PS method. In this paper, we use the software StaMPS/MTI (Hooper & Zebker, 2007; Hooper et al., 2004, 2007) to identify PS pixels and extract deformation signatures.

StaMPS/MTI first identifies PS candidates (PSC) using the amplitude dispersion index, D_A, defined as (Ferretti et al., 2000)

$$D_A \equiv \frac{\sigma_A}{\mu_A} \tag{1}$$

where σ_A and μ_A are the standard deviation and the mean of a series of amplitude values. In general, a threshold value of D_A is adopted to select PSC, and the number of PSC increases with the threshold value.

For example, Ferretti et al. (2001) and Hooper et al. (2007) adopted threshold values of 0.25 and 0.40, respectively. It turns out that use of 0.25 over CRAF leads to severe reduction of PSC pixels. Therefore, we adopted a threshold value $D_A = 0.4$ in this paper. That is, any pixel with $D_A < 0.4$ is considered a PSC.

PS pixels were then selected from PSC pixels based on the noise levels of PSC. To this end, we express the phase from the x-th point in the i-th interferogram as (Ferretti et al., 2001; Hooper et al., 2007):

$$\phi_{x,i} = \phi_{def,x,i} + \phi_{\alpha,x,i} + \phi_{orb,x,i} + \phi_{\varepsilon,x,i} + n_{x,i} \qquad (2)$$

where the right side contains phase contributions from surface deformation ϕ_{def}, atmosphere delay ϕ_{α}, orbit error ϕ_{orb}, look angle error (DEM error, ϕ_{ε}) and noise (thermal effect, co-registration etc., n). Using the error characteristics of the individual terms in Eq. (2), Hooper et al. (2007) define a measure of the variation of the residual phase for a pixel as

$$\gamma_x = \frac{1}{N} \left| \sum_{i=1}^{N} exp\left\{ \sqrt{-1}\left(\phi_{x,i} - \tilde{\phi}_{x,i} - \Delta\hat{\phi}_{\varepsilon,x,i}^u \right) \right\} \right| \qquad (3)$$

where N is the number of interferogram, $\tilde{\phi}_{x,i}$ is a wrapped estimate of the spatially correlated parts of each of the terms on the right side of Eq. (2), and $\Delta\hat{\phi}_{\varepsilon,x,i}^u$ denotes the spatially uncorrelated part of $\phi_{\varepsilon,x,i}$. In this paper, we adopt $\gamma_x = 0.005$ as the threshold. Any PSC pixel with $\gamma_x < 0.005$ is considered a PS pixel. A sufficient spatial PS density (5–10 pixels per km²) is required to properly estimate and remove atmospheric heterogeneity (Colesanti et al., 2003). Over CRAF, it turns out we can identify up to 107 PS pixels per km² (see Section 3) by StaMPS/MTI.

In general, at least 25 images are needed to identify PS pixels (Colesanti et al., 2003). With StaMPS/MTI, the needed number of images can be reduced to about 13 (Hooper et al., 2007). In this paper, we used 20 images from August 2006 to September 2008 to estimate vertical displacements over CRAF (Table 2). Based on baseline lengths and time spans, the master image was chosen to be Image No.7. The maximum perpendicular baseline length is 857.7 m. All the SAR images used in this paper were obtained from the satellite mission ENVISAT operated by the European Space Agency.

Table 2
Information of the ASAR images from Track 232, Frame 3123 of ENVISAT.

Image no.	Orbit	Year	Month	Day	Baseline[a] (m)	Time[b] (days)	Category of image
1	23,332	2006	8	17	857.7	245	Slave
2	23,833	2006	9	21	−690.4	210	Slave
3	24,334	2006	10	26	−347.9	175	Slave
4	25,336	2007	1	4	326.4	105	Slave
5	25,837	2007	2	8	−75.7	70	Slave
6	26,338	2007	3	15	268.8	35	Slave
7	26,839	2007	4	19	0	0	Master
8	27,340	2007	5	24	−63.8	35	Slave
9	27,841	2007	6	28	26.5	70	Slave
10	28,342	2007	8	2	−113.6	105	Slave
11	28,843	2007	9	6	160.4	140	Slave
12	29,344	2007	10	11	−186.8	175	Slave
13	29,845	2007	11	15	217.2	210	Slave
14	30,346	2007	12	20	−277.7	245	Slave
15	30,847	2008	1	24	−47.2	280	Slave
16	31,348	2008	2	28	−260.0	315	Slave
17	32,350	2008	5	8	44.5	385	Slave
18	32,851	2008	6	12	124.5	420	Slave
19	33,853	2008	8	21	62.6	490	Slave
20	34,354	2008	9	25	−120.3	525	Slave

[a] Length of perpendicular baseline component.
[b] Time difference relative to the master image.

3. Result from persistent scatterer interferometry (PSI)

Fig. 3 shows the PSI-derived line-of-sight (LOS) displacements from the 20 SAR images. The unwrapped interferograms from the 19 interferograms were stacked to obtain the mean LOS displacement rates over the 2006–2008 period (Fig. 4). For consistency with the leveling data, the incident angles of radar were used to convert the LOS displacements to vertical ones under the assumption of zero horizontal motion. This assumption has been made in a number of other InSAR subsidence studies (e.g. Amelung et al., 1999; Galloway et al., 1998). However, horizontal displacements do exist in areas with vertical motions induced by groundwater extraction and may be propagated into the PSI-derived vertical motions. If SAR images from ascending and descending tracks are available over the region of interest, it is possible to derive horizontal displacements (Galloway & Hoffmann, 2007). However, since only the images from the ENVISAT descending arc were used in this paper, no horizontal motion was estimated, and the assumption ignores the horizontal motion in the LOS-to-vertical motion conversion is necessary. Table 3 demonstrates the east–west and north–south horizontal displacement rates and GPS-derived LOS displacement at five continuous GPS stations (shown in Fig. 5) over CRAF. These GPS-derived LOS displacements were computed using the method of Yen (Yen et al., 2008) and can be regarded as errors in the PSI-derived LOS velocities due to neglecting horizontal displacements. These errors range from 0.4 to 2.8 mm/year, which are below the noise level of the PSI result. Another example of transformation between GPS and INSAT LOS displacements is given by Huang et al. (2006), who also present a detailed comparison between height changes from leveling and INSAR in an active folding in southern Taiwan.

The scattered vertical rates from PSI were then re-sampled onto a 250×250 m grid (Fig. 5). For comparison, the vertical displacement rates from leveling (see Fig. 2) were also re-sampled on the same 250×250 m grid. Both Fig. 5 (PSI) and Fig. 6 (leveling) show similar spatial patterns of surface deformation, but the former contains more details due to a higher point (pixel) density (see Section 4). Like leveling, PSI (Fig. 5) identifies three townships with major deformation along THSR, i.e., Hsichou, Huwei and Tuku. The implication is that PSI can deliver a promising and fast result of surface deformation over this highly safety-sensitive area of THSR to remove public concern. Also, PSI identifies a zone of major subsidence not detected by leveling: a coastal area in the Mailiao Township of Yunlin, centered at latitude = 23°47′ and longitude = 120°10′. This area is a man-made polder and is the location of the largest oil refinery plant operated by Formosa Plastics Corporation.

For accuracy assessment of the PSI-derived result, we compared the vertical displacement rates on 294 benchmarks determined by leveling and by PSI. Fig. 7 shows the distribution of the benchmarks and the distribution of the differences. The RMS value of the differences is 0.6 cm/year. Of the 294 differences, 257 values (absolute) are less than 1 cm/year, other values are between 1 and 2 cm/year. This suggests that 87.7% of the PSI-derived rates reach an accuracy of 1 cm/year. As shown in boxes A, B, C and D in Fig. 7, the benchmarks with differences of about 1–2 cm/year are located near coasts, riversides or borders of the images. Table 4 summarizes the possible causes of the large differences (see also the point distribution in Fig. 6). The two leading causes are large water vapor effect and interpolation error, followed by edge effect. These causes in Table 4 are empirical and are mostly based on the analysis of Zebker et al. (1997), who found that changes of humidity in space and time will lead to errors in the INSAR-derived deformation up to nearly 10 cm. The boxes of Table 3 and Fig. 7 cover coasts, fishing ponds and rivers, and are very likely subject to humidity changes and therefore large errors in the PSI result.

Hung et al. (2010) attempted to derive vertical deformation over CRAF using DInSAR by stacking interferograms from several SAR ENVISAT images to reduce the effect of atmospheric heterogeneity. The DInSAR result shows that, in the urban area of CRAF, the RMS
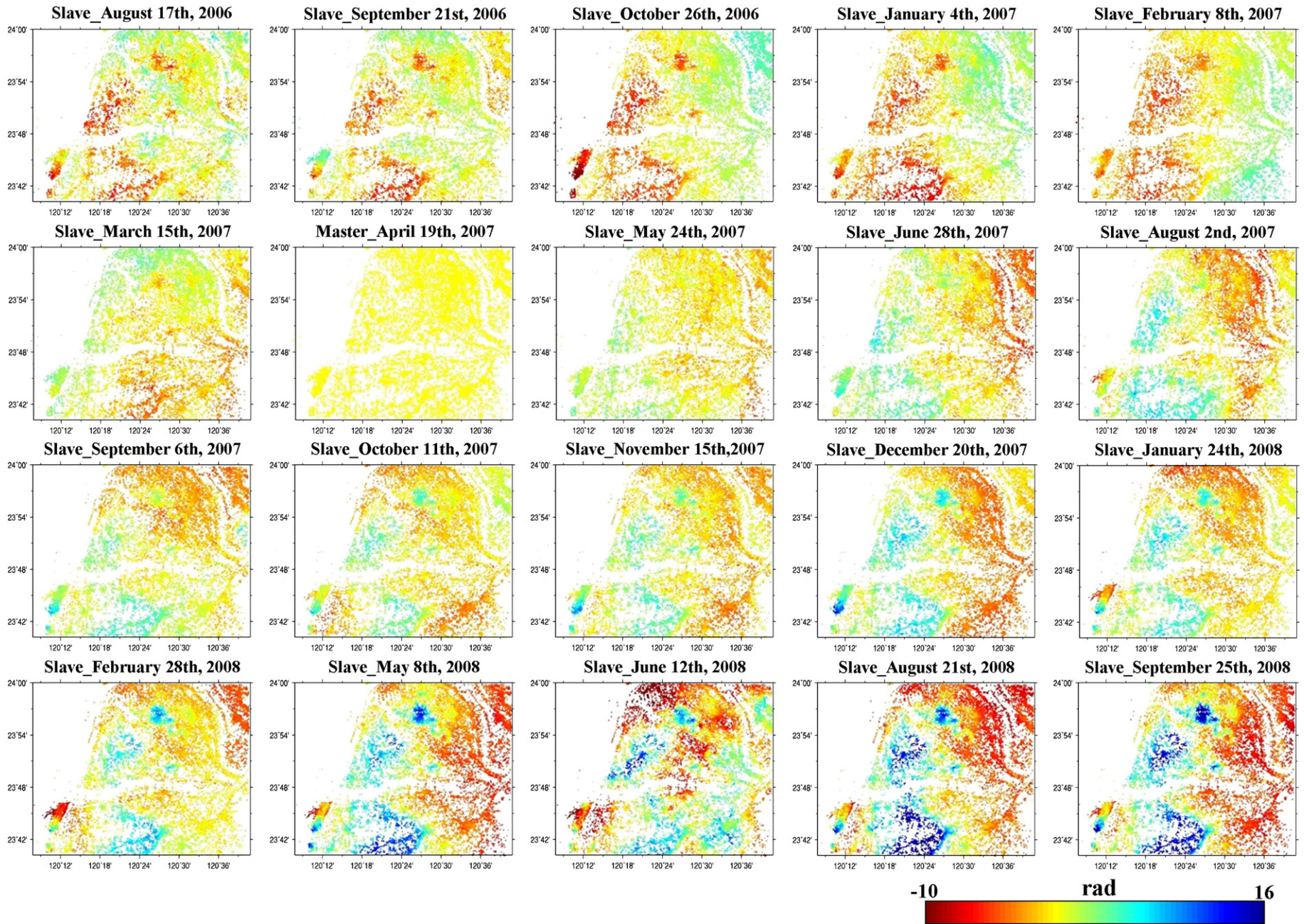
Fig. 3. LOS displacements from 19 slave images relative to the epoch of the master image (April 19, 2007).
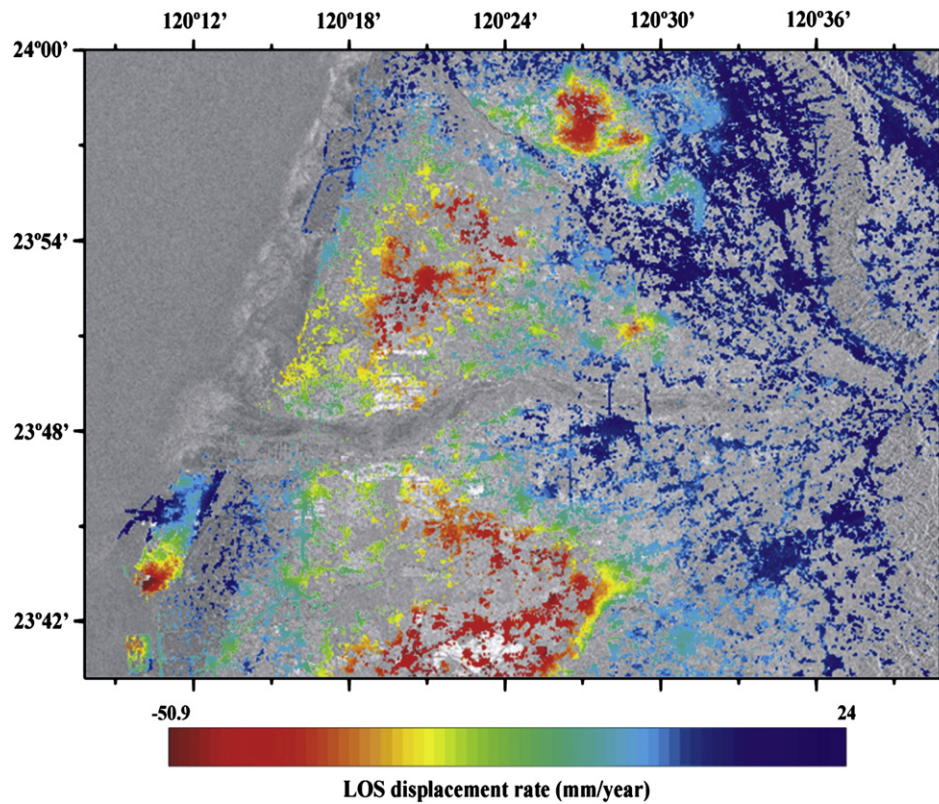
Fig. 4. LOS displacement rates from PSI over 2006–2008.

differences between the DInSAR-derived and leveling-derived vertical displacement rates range from 1 to 2 cm/year. However, DInSAR has a deficiency in accuracy over coastal areas of CRAF, where the DInSAR result differs from the leveling result by as much as 4 cm/year. It was found that the main cause of such large differences in DInSAR is atmospheric heterogeneity. On the other hand, the PSI-derived result given in this paper has a uniform accuracy over the entire CRAF area and is less affected by atmospheric heterogeneity.

4. Fusion of PSI and leveling-derived vertical displacements

The vertical displacements from PSI and leveling were integrated to obtain an optimal field. Leveling refers to orthometric height (height above geoid) and INSAR refer to ellipsoidal height (height above ellipsoid). Because orthometric height is the difference between ellipsoidal height and geoidal height and the geoid does not change (to the sub-mm level) over time, the rate of ellipsoidal height change from PSI and the rate of orthometric height change from leveling at the same spot will be the same (at the sub-mm/year level). The overlapping area between the PSI and leveling-covered zones, shown as the red box in Fig. 2, is 1522.5 km^2, excluding the sea.

Table 3
East–west and north–south horizontal displacement rates and GPS-derived LOS displacement at five continuous GPS stations.

Station Name	Longitude (°)	Latitude (°)	E–W rate (mm/year)	N–S rate (mm/year)	GPS-derived LOS displacement (mm/year)
YSLL	120.222	23.739	1.7	−5.7	1.1
CHSG	120.289	23.860	2.3	−4.9	1.3
TKJS	120.390	23.688	3.4	−4.7	1.7
GFES	120.402	23.741	5.2	−10.5	2.8
HNES	120.479	23.948	2.5	6.8	0.4

Leveling and PSI deliver point-wise and pixel-wise vertical displacements, and the former is about 10 times more accurate than the latter (mm vs. cm in the studied area, see Section 3). The number of PS pixels is about 153,413 in the box of Fig. 2, leading to a density of 107.6 pixels/km^2. The number of leveling benchmarks is 294, resulting in a density of 0.19 points/km^2. If the benchmarks are regarded as pixels, the density of PSI observations is about 530 times higher than that of leveling observations. The combined field should be one that retains the features of both fields, but allows some degree of compromise.

Several methods can be used in such a data fusion. We choose to use a simple "draping" method that considers the higher-precision, lower point-density leveling result as a smoothed correction to the lower-precision, higher point (pixel)-density PSI result. Such a method is frequently used in the earth science community when space-borne data and terrestrial data are merged. For example, Forsberg and Skourup (2005) merged satellite altimeter-derived and terrestrial gravity anomalies using the draping method. Based on the concept of draping, the steps of integrating leveling and PSI-derived vertical displacements are listed below (see Fig. 8). The notations in Fig. 8 are also explained below.

Step 1 Interpolate pixel-wise vertical rates of PSI ($P\Delta H_{psi-all}$) on a 250×250 m grid ($S\Delta H_{PSI250}$)

Step 2 Interpolate the vertical rates ($P\Delta H_{PSI}^i$) at the benchmarks from the grid ($S\Delta H_{PSI250}$)

Step 3 Subtract the PSI-derived rates ($P\Delta H_{PSI}^i$) from the leveling-derived rates ($P\Delta H_{Leveling}^i$) at the benchmarks to obtain the differences $P\Delta H_{LP}^i$

Step 4 Interpolate the differences ($P\Delta H_{LP}^i$) on a 250×250 m grid ($S\Delta H_{LP250}$)

Step 5 Sum the grids of PSI (Step 1) and the grid of difference (Step 4) to form a grid of combined PSI-leveling vertical rates ($F\_S\Delta H_{LP250}$).
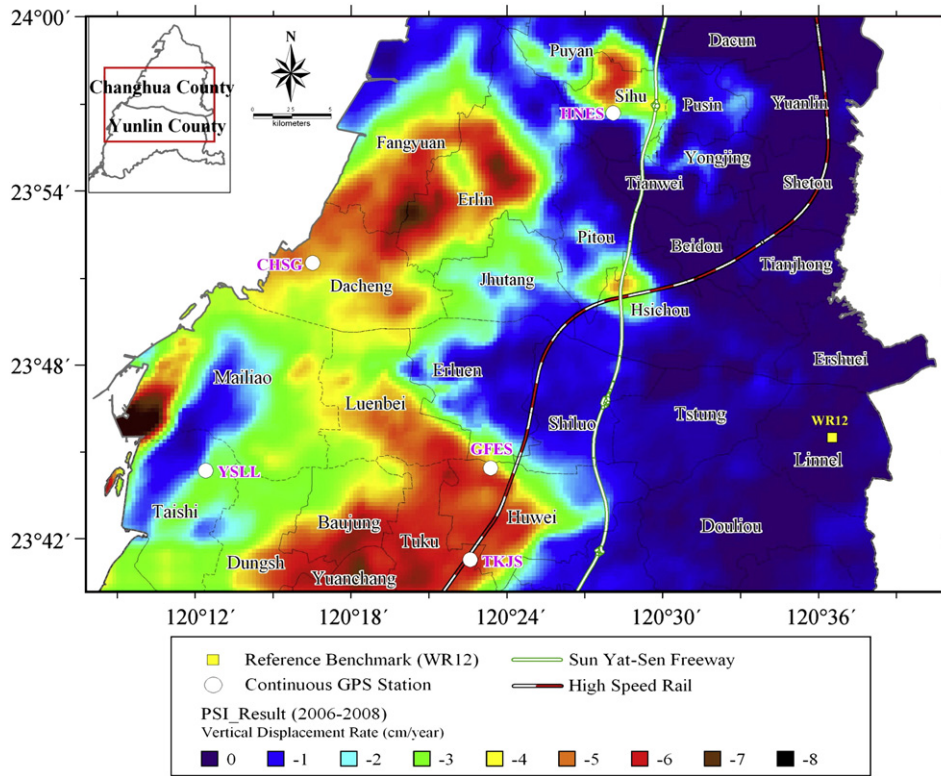
Fig. 5. Vertical displacement rate from PSI over 2006–2008. White circles represent continuous GPS stations where LOS velocities are computed from GPS.

Several methods can be used for the interpolations in the fusion of the PSI and leveling results. For example, minimum curvature (Watson, 1992), Kriging (Cressie, 1993) and least-squares collocation (Moritz, 1980) are three popular methods of interpolation in the earth science community. In this paper, we chose to use Kriging for interpolation. Kriging is a geostatistical method which was used in as
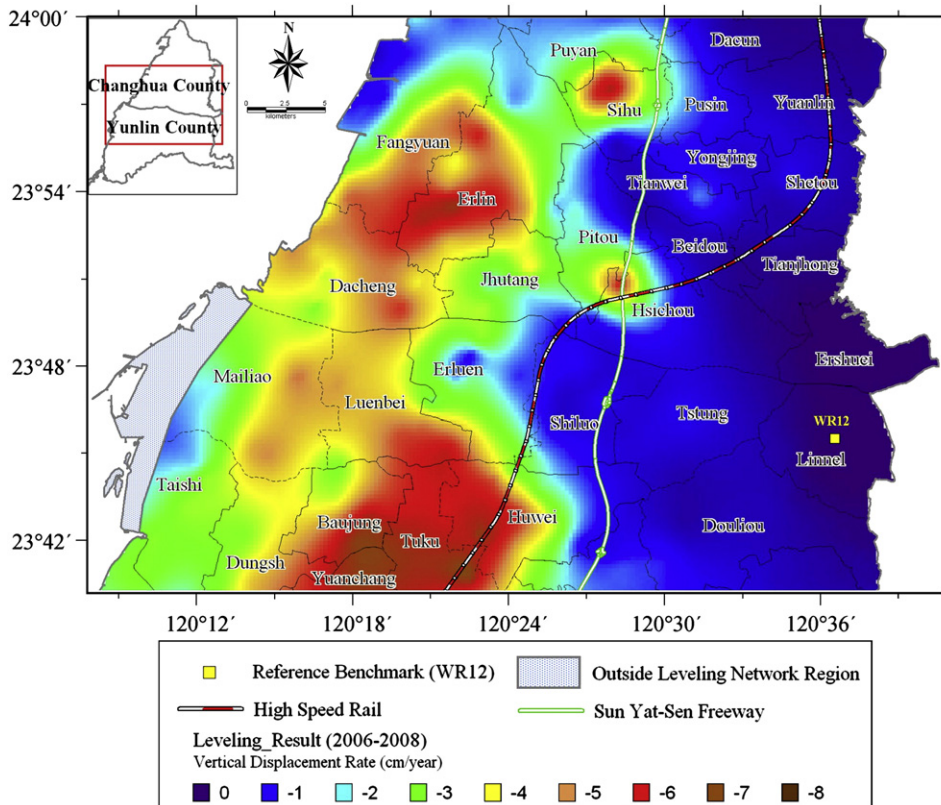

Fig. 6. Vertical displacement rate derived from leveling over 2006–2008.
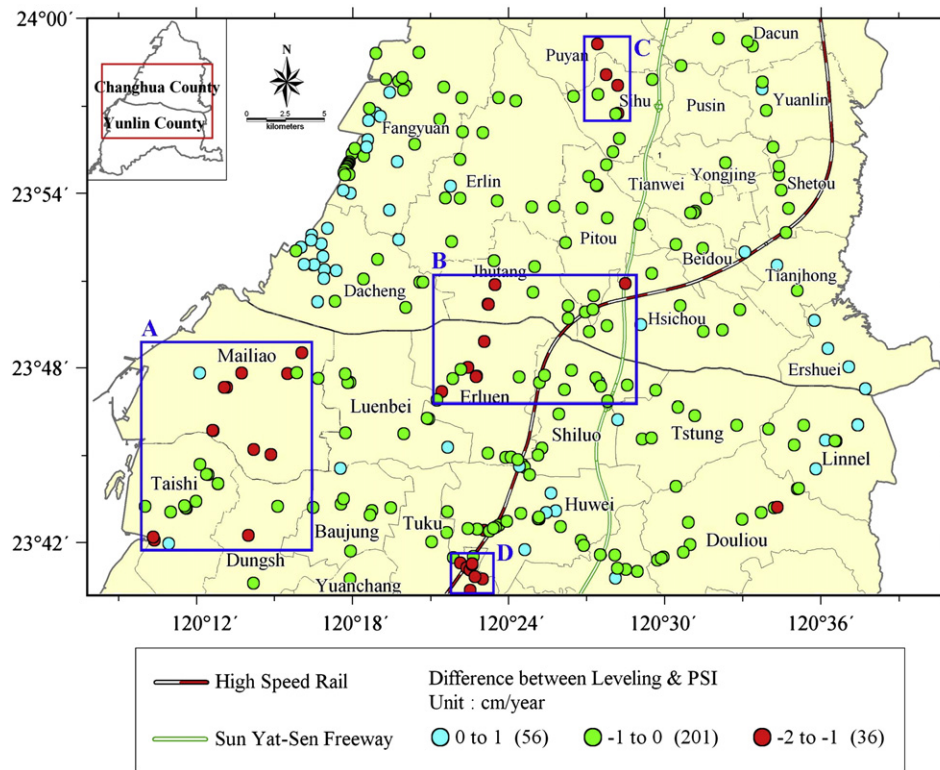
Fig. 7. Differences between the vertical displacement rates from PSI and those from leveling. Circles represent leveling benchmarks in Fig. 4. The blue boxes show areas with differences >1 cm.

early as 1960s, e.g., Matheron (1963), and is more recently described by Diggle and Ribeiro (2007). For the Kriging interpolations carried out in the fusion, the software "Variowin" (Pebesma, 1996) was used. "Variowin" estimates the influence range and sill of a given variogram model using the goodness of fit between model values and observations. In this paper, we used the index exponential function as the variogram model.

The combined vertical rates are given in Fig. 9. Fig. 10 shows the differences between the combined vertical rates and the leveling-derived vertical rates at the same benchmarks as those given in Fig. 7. The RMS difference is reduced from 0.6 cm/year (PSI minus leveling) to 0.4 cm/year (combined minus leveling). Some features about the combined field are listed below:

(1) It reveals the same spatial pattern as those in the contributing fields.
(2) The combined field reproduces the vertical rates of PSI and leveling to within ± 1 cm/year.
(3) The void zone in the leveling field (see the coastal zone centered at latitude = 23°47′ and longitude = 120°10′, Figs. 5 and 6) is filled by the PSI field.
(4) Large errors in the PSI solution are reduced in the combined field.

Table 4
Summary of causes of large difference (>1 cm/year) in PSI-derived vertical rate.

Area	Causes
A	1. Large wet tropospheric delays due to fishing ponds and Taiwan Strait
	2. Interpolation error due to sparse PSI points
B	1. Large wet tropospheric delays due to Choushui River and paddy fields
	2. Interpolation error due to sparse PSI points
C	1. Large error due to edge effects of SAR images
	2. Interpolation error due to sparse PSI points
D	1. Large error due to edge effects of SAR images
	2. Interpolation error due to sparse PSI points

Therefore, the combined field is more representative of overall deformation characteristics than the PSI-only or leveling-only field, and it is better suited for the assessment of the impact of subsidence over CRAF.

5. Discussion and conclusions

With 20 ENVISAT SAR images over 2006–2008 and the software StaMPS/MTI, the PSI technique was used to derive vertical displacements over CRAF. The PSI-derived vertical displacement rates agree with those from leveling to 0.6 cm/year (RMS), and their accuracies are more uniform over the entire CRAF as compared to the DInSAR result. In comparison to leveling, PSI provides a more detailed spatial and temporal coverage in subsidence monitoring. The PSI result shows that THSR passes through three major subsidence areas in three townships in Yunlin County, where the maximum annual subsidence is 7 cm. Also, PSI detects a zone of major subsidence in the coastal industrial area of Yunlin, which is not seen in the leveling result. Information like this will be vital to decision making for the Taiwan government when dealing with the THSR safety issue.

Our data fusion method is effective in merging the leveling and PSI-derived results. The merged field better represents the overall subsidence pattern, provides more subsidence details and agrees better with the leveling result than the original sources. For future studies of fusion, one may employ an improved method that uses the wavelet functions or spectral combinations to represent the space-borne and terrestrial data in the fusion.

Although the PSI result in this paper is promising, there are still large errors exceeding 1 cm/year over certain areas. These large errors may be reduced using results from continuous GPS stations placed in these areas. The idea is to model atmospheric delays from continuous GPS measurements, which are then used to correct for the atmospheric effects in the radar interferograms. Furthermore, currently leveling in the studied area is carried out only once a year (the leveling surveys for the PSI validation were carried out in October 2006, July 2007 and May 2008), and this low temporal sampling result

$S\Delta H_{PSI\_points}$

Kriging Interpolation

$S\Delta H_{PSI\,250}$

To read the changing rate of the $S\Delta H_{PSI\,250}$ at the corresponding benchmark of $P\Delta H_{PSI}^i$

$P\Delta H_{Leveling}^i$

$P\Delta H_{PSI}^i$

$P\Delta H_{LP}^i = P\Delta H_{Leveling}^i - P\Delta H_{PSI}^i$

Kriging Interpolation

$S\Delta H_{LP\,250}$

$F\_S\Delta H_{LP250} = S\Delta H_{PSI\,250} + S\Delta H_{LP\,250}$
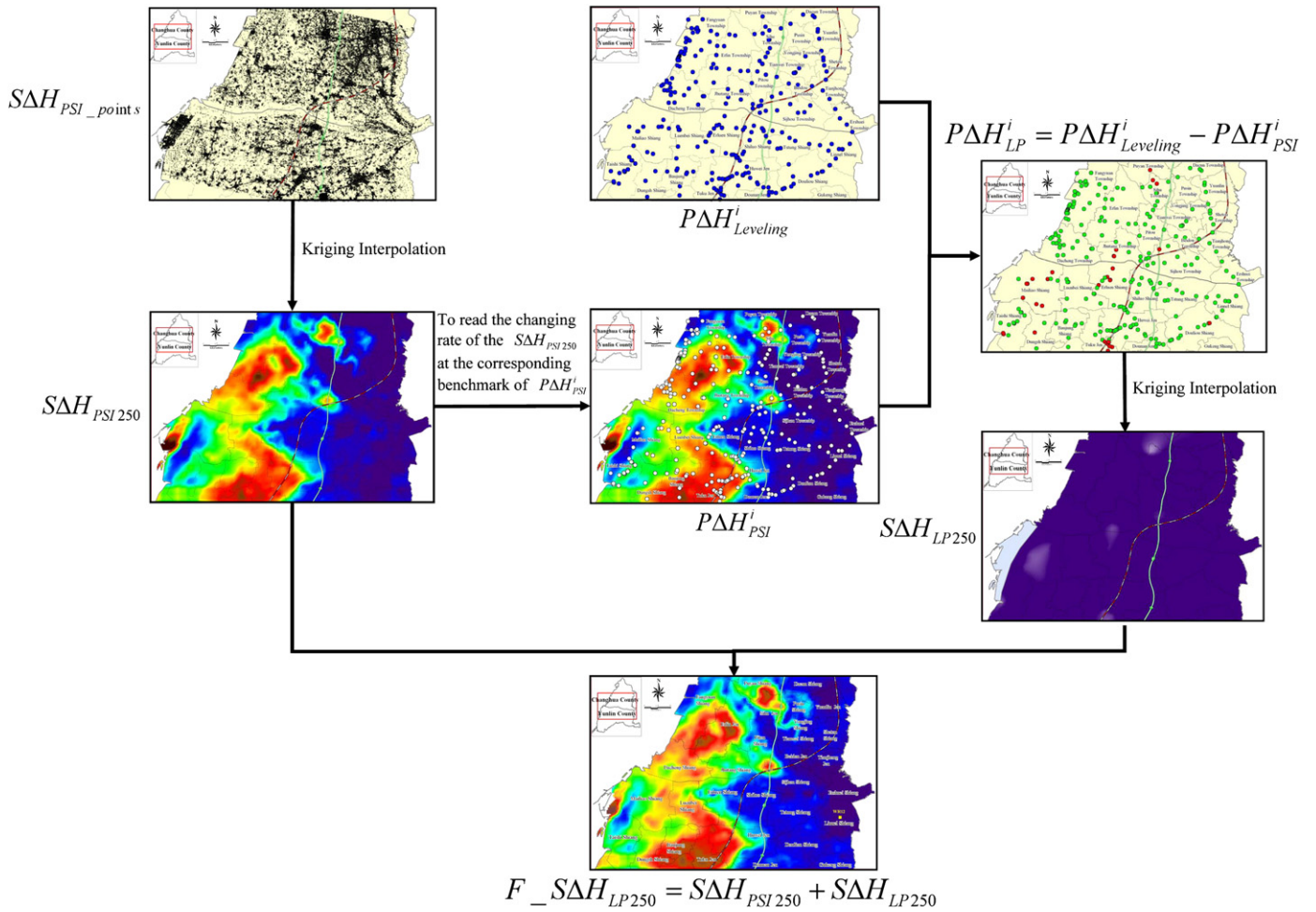
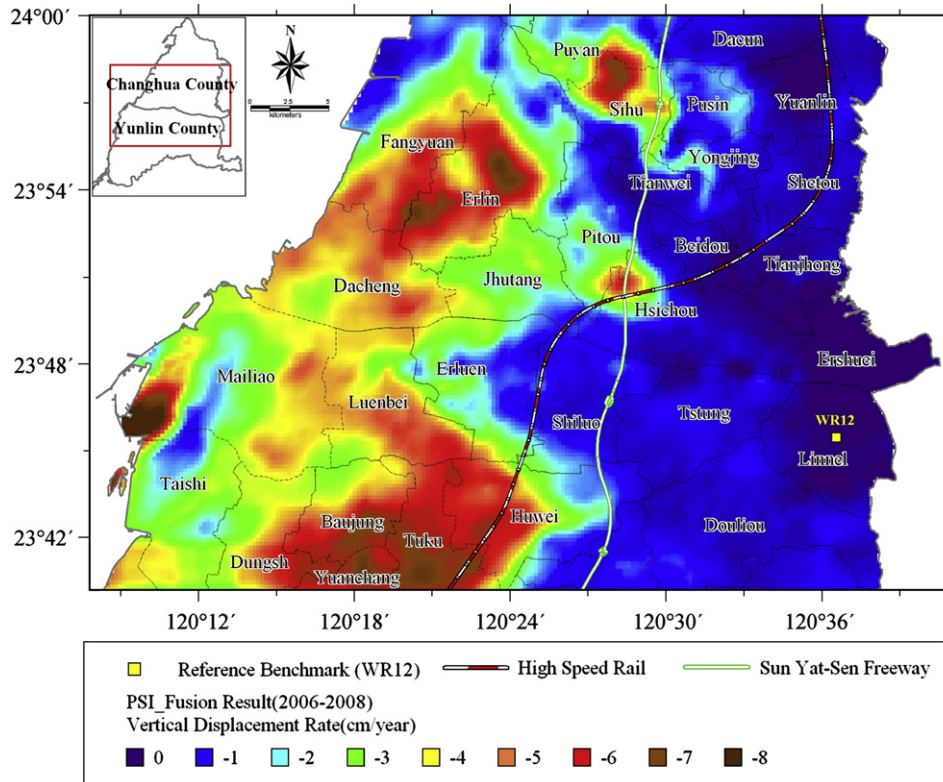Fig. 8. The flowchart for fusion of leveling and PSI-derived vertical displacements.

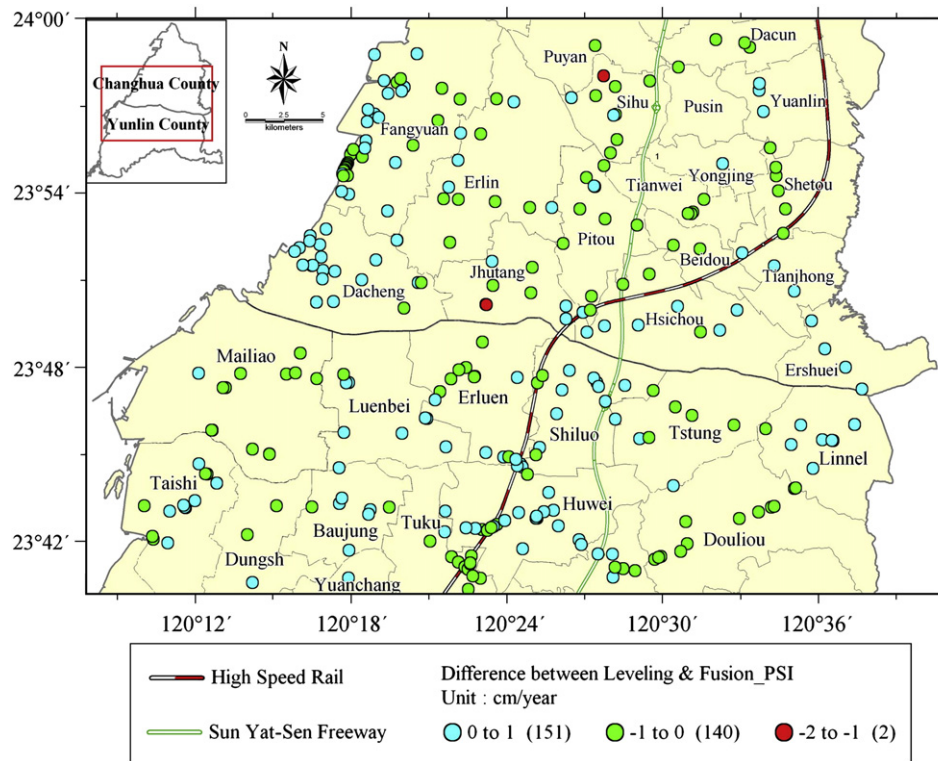Fig. 9. Vertical displacement rates from PSI and leveling over 2006–2008.

Fig. 10. Differences in the vertical displacement rate between the combined field and the leveling-only field. Circles represent leveling benchmarks in Fig. 4.

cannot be used to validate the 35-day vertical deformations from ENVISAT. This problem of validation can again be overcome by using the high-rate (daily) vertical deformations from continuous GPS. Considering the active tectonic motion in Taiwan, it will be highly desirable to carry out an island-wide determination of high-rate (at 35-day interval with ENVISAT) surface deformation using PSI, and the result can be validated by the result from some of the 300 continuous GPS stations in Taiwan (Kuo, 2008; Lin et al., 2010).

References

Abidin, H. Z., Djaja, R., Darmawan, D., Akbar, A., Rajiyowiryono, H., Sudibyo, Y., et al. (2001). Land subsidence of Jakarta (Indonesia) and its geodetic monitoring system. *Natural Hazards*, 23, 365−387.

Amelung, F., Galloway, D. L., Bell, J. W., Zebker, H. A., & Laczniak, R. J. (1999). Sensing the ups and downs of Las Vegas: InSAR reveals structural control of land subsidence and aquifer-system deformation. *Geology*, 27(6), 483−486.

Berardino, P., Fornaro, G., Lanari, R., & Sansosti, E. (2002). A new algorithm for surface deformation monitoring based on small baseline differential SAR interferograms. *IEEE Transactions on Geoscience and Remote Sensing*, 40(11), 2375−2383.

Chang, C. P., Wang, C. T., Chang, T. Y., Chen, K. S., Liang, L. S., Pathier, E., et al. (2004). Application of SAR interferometry to a large thrust deformation: the 1999 Mw = 7.6 Chichi earthquake in central Taiwan. *Geophysical Journal International*, 159, 9−16.

Colesanti, C., Ferretti, A., Novali, F., Prati, C., & Rocca, F. (2003). SAR monitoring of progressive and seasonal ground deformation using the permanent scatterers technique. *IEEE Transactions on Geoscience and Remote Sensing*, 41(7), 1685−1701.

Cressie, N. A. C. (1993). *Statistics for spatial data.* A Wily-Interscience Publication. John Wiley & Son, Inc.

Diggle, P. L., & Ribeiro, P. J. (2007). *Model-based geostatistics.* Berlin: Springer 230 pp.

Ferretti, A., Prati, C., & Rocca, F. (2000). Nonlinear subsidence rate estimation using permanent scatterers in differential SAR interferometry. *IEEE Transactions on Geoscience and Remote Sensing*, 38, 2202−2253.

Ferretti, A., Prati, C., & Rocca, F. (2001). Permanent scatterers in SAR interferometry. *IEEE Transactions on Geoscience and Remote Sensing*, 39(1), 8−20.

Forsberg, R., & Skourup, H. (2005). Arctic Ocean gravity, geoid and sea-ice freeboard heights from ICESat and GRACE. *Geophysical Research Letters*, 32(21), L21502, doi:10.1029/2005GL023711

Gabrysch, R. K., & Ronald, J. N. (2005). Measuring a century of subsidence in the Houston–Galveston region, Texas, USA. *Proc., 7th International Symposium on Land Subsidence, Shanghai (CN)*.

Galloway, D. L., & Hoffmann, J. (2007). The application of satellite differential SAR interferometry-derived ground displacements in hydrogeology. *Hydrogeology Journal*, 15(1), 133−154, doi:10.1007/s10040-006-0121-5

Galloway, D. L., Hudnut, K. W., Ingebritsen, S. E., Phillips, S. P., Peltzer, G., Rogez, F., et al. (1998). Detection of aquifer system compaction and land subsidence using interferometric synthetic aperture radar, Antelope Valley, Mojave Desert, California. *Water Resources Research*, 34(10), 2573−2585.

Gong, S. L., & Yang, S. L. (2008). Effect of land subsidence on urban flood prevention engineering in Shanghai. *The Key Magazine of China Technology*, 39(6), 1−20.

Hanson, R. T., Zhen, L., & Faunt, C. (2005). Simulation of subsidence for the regional-aquifer system in the Santa Clara Valley, California. *Proc., 7th International Symposium on Land Subsidence, Shanghai (CN)*.

Hashimoto, M., Enomoto, M., & Fukushima, Y. (2009). Coseismic deformation from the 2008 Wenchuan, China, earthquake derived from ALOS/PALSAR images. *Tectonophysics*, doi:10.1016/j.tecto.2009.08.034

Hooper, A., Segall, P., & Zebker, H. (2007). Persistent scatterer interferometric synthetic aperture radar for crustal deformation analysis, with application to Volcán Alcedo, Galápagos. *Journal of Geophysical Research*, 112, B07407, doi:10.1029/2006JB004763

Hooper, A., & Zebker, H. (2007). Phase unwrapping in three dimensions with application to InSAR time series. *Optical Society of America*, 24(9), 2737−2747.

Hooper, A., Zebker, H., Segall, P., & Kampes, B. (2004). A new method for measuring deformation on volcanoes and other natural terrains using InSAR persistent scatterers. *Geophysical Research Letters*, 31(23), 611−615.

Huang, M. H., Hu, J. C., Hsieh, C. S., Ching, K. E., Rau, R. J., & Pathier, E. (2006). A growing structure near the deformation front in SW Taiwan deduced from SAR interferometry and geodetic observation. *Geophysical Research Letters*, 33, L12305, doi:10.1029/2005GL025613

Hung, W. C., Hwang, C., Chang, C. P., Yen, J. Y., Liu, C. H., & Yang, W. H. (2010). Monitoring severe subsidence in Taiwan by multi-sensors: Yunlin, the southern Choushui River Alluvial Fan. *Earth Science Geology*, 59, 1535−1548.

Hung, W. C., & Liu, C. S. (2007). Taiwan land subsidence monitoring and surveying analysis. *Report of Industrial Technology Research Institute (ITRI), Hsinchu* 335 pp. (in Chinese).

Hwang, C., Hung, W. C., & Liu, C. H. (2008). Results of geodetic and geotechnical monitoring of subsidence for Taiwan High Speed Rail operation. *Natural Hazards*, 47, 1−16.

Kampes, B. M. (2005). Displacement parameter estimation using permanent scatterer interferometry. Ph.D. thesis. Delft University of Technology.

Kuo, L. C. (2008). The network service of automatic GPS analysis system and geo-science research (in Chinese). *Technique report of Academic Sinica* 9 pp.

Lin, K. C., Hu, J. C., Ching, K. E., Angelier, J., Rau, R. J., Yu, S. B., et al. (2010). GPS crustal deformation, strain rate and seismic activity after the 1999 Chi-Chi earthquake in Taiwan. *Journal of Geophysical Research*, 115, B07404, doi:10.1029/2009JB006417

Lyons, S., & Sandwell, D. (2003). Fault creep along the southern San Andreas from interferometric synthetic aperture radar, permanent scatterers, and stacking. *Journal of Geophysical Research*, 108(B1), 2047−2070.

Ma, R., Wang, Y. X., Ma, T., Sun, Z. Y., & Yan, S. L. (2006). The effect of stratigraphic heterogeneity on area distribution of land subsidence at Taiyuan, northern China. *Journal of Environment Geology*, *50*(4), 551−568.

Matheron, G. (1963). Principles of geostatistics. *Economic Geology*, *58*, 1246−1266.

Moritz, H. (1980). *Advanced physical geodesy.* Tunbridge Wells: Abacus Press 500 pp.

Motagh, M., Djamour, Y., Walter, T. R., Wetzel, H. -U., Zschau, J., & Arabi, S. (2007). Land subsidence in Mashhad Valley, northeast Iran: results from InSAR, levelling and GPS. *Geophysical Journal International*, *168*(2), 518−526.

National Yunlin University of Science and Technology (2009). *The feasibility study of multiple water resource development demands in Yunlin County.* Taipei: Water Resources Agency, Ministry of Economic Affairs 60 pp.

Noppadol, P. W., Giao, P. H., & Nutalaya, P. (2006). Land subsidence in Bangkok, Thailand. *Engineering Geology*, *82*, 187−201.

Osmanoglu, B., Dixon, T. H., Wdowinski, S., Enrique, C. -C., & Jiang, Y. (2010). Mexico city subsidence observed with persistent scatterer InSAR. *Journal of Applied Earth Observation and Geoinformation*, doi:10.1016/j.jag.2010.05.009

Pebesma, Y. (1996). *VARIOWIN: Software for spatial data analysis in 2D.*New York: Springer-Verlag 91 pp.

Sato, C., Haga, M., & Nishino, J. (2006). Land subsidence and groundwater management in Tokyo. *International Review for Environmental Strategies*, *6*(2), 403−424.

Tosi, L., Teatini, P., Carbognin, L., & Frankenfield, J. (2007). A new project to monitor land subsidence in the northern Venice Coastland (Italy). *Journal of Environmental Geology*, *52*, 889−898.

Watson, D. F. (1992). *Contouring: A guide to the analysis and display of spatial data.* Pergamon Press.

Yen, J. Y., Chen, K. S., Chang, C. P., & Boerner, W. M. (2008). Evaluation of earthquake potential and surface deformation by differential interferometry. *Remote Sensing of Environment*, *112*(3), 782−795.

Zebker, H. A., Rosen, P. A., & Hensley, S. (1997). Atmospheric effects in interferometric synthetic aperture radar surface deformation and topographic maps. *Journal of Geophysical Research*, *102*, 7547−7563.